8-15-2018

Experimental and Modeling Study of Compressive Creep In 3D-Woven Ni-Based Superalloys

Hoon-Hwe Cho
Northwestern University

Dinc Erdeniz
Marquette University, dinc.erdeniz@marquette.edu

Keith W. Sharp
TexTech Industries, Inc.

David C. Dunand
Northwestern University

Mechanical Engineering Faculty Research and Publications/College of Engineering

Experimental and Modeling Study of Compressive Creep In 3D-Woven Ni-Based Superalloys

Hoon-Hwe Cho
Department of Materials Science and Engineering, Northwestern University, Evanston, IL
Dinc Erdeniz
Department of Materials Science and Engineering, Northwestern University, Evanston, IL
Keith W. Sharp
TexTech Industries, Inc., 1 City Center, Portland, ME, 04101
David C. Dunand
Department of Materials Science and Engineering, Northwestern University, Evanston, IL

Abstract

Micro-architectured Ni-based superalloy structures, with Ni-20Cr-3Ti-2Al (wt.%) composition and γ/γ'-microstructure, are created by a multi-step process: (i) non-crimp orthogonal 3D-weaving of ductile, 202 μm diameter Ni-20%Cr wires, (ii) gas-phase alloying with Al and Ti, (iii) simultaneous transient-liquid phase (TLP)

bonding between wires and homogenization within wires *via* interdiffusion, (iv) solutionizing to create a single-phase solid solution, and (v) aging to precipitate the γ' phase. The creep behavior of these 3D-woven γ/γ' nickel-based superalloys is studied under uniaxial compression *via* experiments at 825 °C and *via* finite element (FE) analysis, using a 3D model of the woven structures obtained through X-ray micro-tomography. The creep strain rate for the woven Ni-based superalloy is higher than that for the bulk superalloy due to the lower solid volume fraction of the woven structure, while the creep exponents are identical. The compressive creep behavior is sensitive to the geometry of the woven structures: fewer wires perpendicular to the load and fewer bonds between wires cause lower creep resistance of the woven structure, due to a reduction in load transfer from the longitudinal wires (which are primarily load-bearing) and the perpendicular wires. Creep buckling of longitudinal wires drastically reduces creep resistance of the woven structure, confirming the importance of maintaining longitudinal wires vertical and parallel to the uniaxial compression direction. Finally, reducing wire cross-section, *e.g., via* oxidation, reduces creep resistance. The oxidation kinetics of the wire structures at 750, 825, and 900 °C displayed parabolic rate constants comparable to commercial Ni-based superalloys, but indicates that up to 35% of the wire cross-section is oxidized after 7 days at 825 °C, such that oxidation-resistant coatings are needed for long-term use in oxidative environment.

Graphical abstract
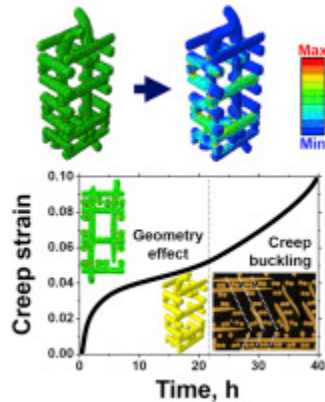
Keywords

Nickel alloys, 3D weaving, Finite element analysis, High-temperature mechanical behavior, Creep buckling

1. Introduction

In recent years, artificially structured materials with stochastic architectures have received significant interest [1,2], not only because of their desirable properties such as low density, and high specific strength, stiffness, and surface area [[3], [4], [5]], but also for their broad range of non-structural applications, including heat/sound absorption, damping, filters, catalyst substrates, and fuel cell interconnects [[6], [7], [8], [9]]. An important characteristic of these structured materials is their ability to optimize various properties in an isotropic or anisotropic manner by topologically tailoring nano/micro-architectures [10]. Some examples of the structured materials with regular micro-architectures are micro-lattice structures [11,12], woven structures [5,13], and topology-optimized lattices [[14], [15], [16]].

Nickel-based superalloys are well suited for structural applications at elevated temperatures up to approximately 1050 °C [[17], [18], [19]]. Fabrication of topologically tailored micro-architectures from Ni-based superalloys can achieve optimized combination of high strength/stiffness and high heat transfer properties for efficient cooling for thermo-structural applications [5,9,20]. Zhao et al. [9] fabricated topologically optimized 3D-woven architectures from Cu and Ni-20Cr wires and examined their permeability in three orthogonal directions

by employing both computational and experimental approaches. They showed that the optimized structures achieved nearly four times higher permeability with minimal reduction in stiffness. Erdeniz et al. [5] reported a process, which is employed in the present work, for the fabrication of 3D-woven Ni-based superalloys with metallurgical bonding between wires by by-passing significant manufacturing hurdles such as limited ductility and difficulty in joining that comes with superalloy wires. They decoupled the weaving and alloying steps by using ductile Ni-20Cr precursor wires for 3D-weaving and post-textile alloying *via* pack cementation. Additionally, Erdeniz et al. [20] demonstrated that the bonding between wires could lead to higher strength at ambient temperature and they developed a technique to use transient-liquid-phase (TLP) bonding for this purpose. In particular, understanding the mechanical behavior of the woven structures at elevated temperatures is very important for thermo-structural applications of Ni-based superalloys with topologically optimized architectures. There are no reports on the high-temperature mechanical behavior, especially creep deformation behavior, of the woven structures consisting of Ni-based superalloy wires.

In the present work, we employ continuum-mechanics simulations to probe creep deformation of 3D-woven structures which allow for a systematic variation of topological and architectural features much more easily than *via* experiments. Based on 3D models of the woven structures previously obtained from X-ray micro-tomography [5] and using experimental creep data of the bulk alloy as input, the creep deformation behavior of the woven Ni-based superalloys is simulated under uniaxial compression *via* finite element (FE) analysis, which is then compared with experimental creep strain data. We also examine the creep deformation behavior by digitally modifying the geometry of the woven structures, such as the number of Z wires and the number of bonds between the wires. Additionally, we consider creep buckling as a potential deformation mechanism, which can cause lower creep resistance of the woven structure under uniaxial compression at elevated temperatures, by employing both computational and experimental approaches.

2. Experimental procedures

2.1. Fabrication of bulk and 3D woven superalloys

A bulk Ni-based superalloy button with a composition of Ni-20Cr-3Ti-2Al was arc melted from Ni-20Cr pellets (99.9% purity), Ti sponges (99.9% purity), and Al pellets (99.9% purity). The button was flipped over five times, after each arc melting sequence that lasted 30 s. The resulting alloy was then solutionized at 1200 °C for 2 h and aged at 900 °C for 16 h. Creep samples were cut out of this button *via* electro-discharge machining (EDM).

The other type of materials used in this study are non-crimp 3D orthogonal woven structures fabricated from soft-annealed Ni–20Cr wires, with a diameter of 202 μm. A detailed description of the weaving process is given in Ref. [5]. Woven samples, cut to a length of 15 mm, a width of 25 mm, and a thickness of 3.5 mm (corresponding to 11 wire layers, with an approximate mass of 7 g), were buried in a pack mixture consisting of 57 wt% Al_2O_3 powders (20–50 μm particle size) as filler, 30 wt% Ti powders (99.5% purity, −325 mesh) and 10 wt% Raney Ni precursor powders (Ni–50 wt% Al, 150 μm particle size) as Al and Ti sources, and 3 wt% NH_4Cl powders (100 μm particle size) as activator. Approximately 40 g of pack was poured in a steel retort, where the internal pressure rises at elevated temperatures, with the cut specimen placed at the center of the retort and fully buried in the pack. The inner wall of the steel retort was spray-coated with boron nitride to minimize contamination. The retort was placed at the water-cooled end of a tube furnace that was heated to 1000 °C. After flushing the furnace tube with Ar for 15 min, the retort was pushed into the hot zone of the furnace, where it was held for 60 min. The retort was then pulled back to the water-cooled end of the tube and cooled there for 15 min. The specimens were removed from the pack and ultrasonicated in acetone for 2 h to remove all pack remnants.

Four layers of the Al- and Ti-coated woven structures were stacked, sandwiched between two superalloy (Inconel X750, 1 mm thickness) sheets, and placed in a jig to hold the sandwich structure together. The jig was then placed in a vacuum furnace and the following heat treatment was carried out: (i) transient liquid phase bonding at 1140 °C for 30 min, (ii) homogenization at 1100 °C for 48 h, (iii) solutionizing at 1200 °C for 2 h, and (iv) aging at 900 °C for 16 h. The bonded sandwich structure was then removed from the furnace and cut with a diamond blade into smaller samples for creep test. The creep samples were intended to have final dimensions of 8 mm × 8 mm x 16 mm. However, due to insufficient bonding between the layers, the sandwich structure fell apart upon cutting and we were only able to obtain creep specimens with dimensions of 8 mm × 8 mm x 7 mm (equivalent of two woven layers).

2.2. Creep testing of bulk and 3D woven superalloys

Compressive creep experiments were performed at 825 ± 2 °C on bulk and woven samples with dimensions of 5 mm × 5 mm x 11 mm and 8 mm × 8 mm x 7 mm, respectively. The samples were placed between silicon carbide platens lubricated with boron nitride and heated in air in a three-zone furnace with the temperature measured using a K-type thermocouple placed within 1 cm of the specimen. They were subjected to uniaxial compression by Ni-based superalloy rams in a compression cage using dead loads. Sample displacement was monitored with a linear variable displacement transducer with a resolution of 6 μm, resulting in a minimum measurable strain increment of 3×10^{-4}. A strain rate was obtained by measuring the slope of the strain vs. time plot in the steady-state (secondary) creep regime. After a measurable steady-state strain rate was achieved, the applied load was increased to obtain another steady-state strain rate. Thus, a single specimen provided minimum creep rates for a series of increasing stress levels, at the end of which the total strain did not exceed 10%.

2.3. Static oxidation tests

Woven samples were tested for their oxidation behavior at three different temperatures (750, 825, 900 °C) up to 1 week (168 h) in static air. Samples, placed in alumina crucibles, were weighed before the tests with an analytical balance with an accuracy of 0.0001 g. Two samples per temperature were held in the furnace for a pre-specified duration (3, 6, 12, 24, 48, 96, 168 h) and weighed again at the end of each step after cooling to room temperature in air. The mass gain data were then used to assess the oxidation kinetics.

2.4. Metallography and microscopy

Samples were polished down to 0.05 μm using standard metallographic techniques. Select specimens were etched with a 33 vol% water +33 vol% acetic acid +33 vol% nitric acid +1 vol% hydrofluoric acid solution to reveal the γ′-Ni_3(Al,Ti) precipitates. An optical microscope and a scanning electron microscope equipped with an energy dispersive X-ray spectrometer were used for microscopic and chemical analyses.

3. Computational model and methodology

3.1. Governing equations

The relationship describing the creep behavior of metallic foams has originally been developed by Gibson and Ashby [21] considering a cubic array of struts subjected to bending deformation. The steady-state creep strain rate $\dot{\varepsilon}^*$ of the foam is expressed by the following equation:

$$(1) \quad \dot{\varepsilon}^* = K \frac{0.6}{(n+2)} \left(\frac{1.7(2n+1)}{n}\right)^n \sigma^{*n} \rho^{*-(3n+1)/2} \exp\left(\frac{-Q}{RT}\right)$$

where σ^* is the uniaxial stress applied to the foam, ρ^* is the relative density of the foam, Q is the activation energy of the bulk metal, R is the gas constant, T is the temperature and the parameters K and n are related to the power-law creep equation, for the solid material of which the foam consists, which is given by:

(2) $\dot{\varepsilon} = K\sigma^n exp(\frac{-Q}{RT})$

where $\dot{\varepsilon}$ is the uniaxial strain rate, K is the Dorn constant, σ is the uniaxial applied stress and n is the stress exponent. The parameters K, n and Q are obtained by minimizing the sum of the squared difference between the measured secondary creep strain rate data of the bulk alloy and the computed data, and these values are listed in Table 1. Fig. 1 shows the measured and calculated secondary creep strain rates of the bulk Ni-20Cr-3Ti-2Al superalloy as a function of uniaxial applied stress. The best-fit line using Eq. (2) provides the stress exponent, and the parameters are listed in Table 1, which are close to those of Ni-Cr superalloys for slightly different compositions [18,[22], [23], [24]], thus making good physical sense.

Table 1. Creep properties used for FE analysis.

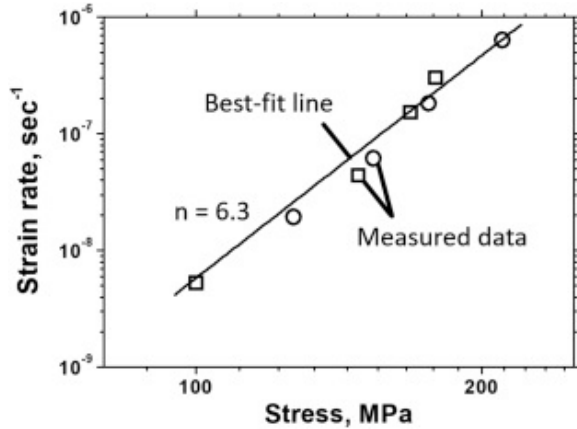| Property/Parameter	Value
Dorn constant (K)	6.9×10^{-5} MPa^{-n} s^{-1}
Stress exponent (n)	6.3
Activation energy (Q)	353 kJ mol^{-1}

Fig. 1. Plot of secondary strain rate measured at 825 °C vs. uniaxial compressive stress for bulk Ni-20Cr-3Ti-2Al superalloys aged to 900 °C (different symbols are for two specimens). The best-fit line to Eq. (2) provides the stress exponent.

The stress increment of Cauchy stress $d\sigma$ can be expressed as:

(3) $d\boldsymbol{\sigma} = \boldsymbol{C}^e : d\boldsymbol{\varepsilon}^e$

with the elastic stiffness tensor $\boldsymbol{C}^e$ and the elastic strain increment $d\boldsymbol{\varepsilon}^e$. The total strain increment $d\boldsymbol{\varepsilon}^t$ is as follows:

(4) $d\boldsymbol{\varepsilon}^t = d\boldsymbol{\varepsilon}^e + d\boldsymbol{\varepsilon}^p + d\boldsymbol{\varepsilon}^c$

where $d\boldsymbol{\varepsilon}^p$ and $d\boldsymbol{\varepsilon}^c$ are the plastic and creep strain increments, respectively. In this work, the creep deformation behavior was only considered, and the effect of plastic deformation is neglected, which is justified by the applied stresses (200 MPa) being well below the yield stresses of Ni-based superalloys with similar compositions (~500–800 MPa) [[25], [26], [27], [28]]. The creep strain increment is obtained from the above equation (4), and consequently, the stress increment is given by:

(5) $d\boldsymbol{\sigma} = \boldsymbol{C}^e : (d\boldsymbol{\varepsilon}^t - d\boldsymbol{\varepsilon}^p - d\boldsymbol{\varepsilon}^c)$

3.2. Finite element modeling

The governing equations and the optimized parameters listed in the previous section are implemented in the ABAQUS/Standard software by employing a user-defined subroutine. The creep test is simulated at 825 °C with applied uniaxial compressive stresses in the range of 50–200 MPa, using Eq. (2) which assumes no primary creep contribution from the material itself.

The representative volume element (RVE) of the woven structure, which is reduced into a half sub-structure, using the symmetry along *y*-axis from the periodic unit cell to compute the creep deformation under uniaxial compression, as illustrated in Fig. 2a. The experimental microstructure is obtained *via* X-ray micro-tomography [5], as seen in Fig. 2b. Based on the experimental microstructure, a surface mesh is produced and then a grid of solid tetrahedral elements is generated using the ABAQUS/CAE software. The RVE consists of 164,285 quadratic, tetrahedral elements (C3D10T), and the solid volume fraction of the RVE is1 32.8% of the total volume of the structure. Mesh sensitivity analysis was carried out for 1 h creep deformation, by increasing the elements from 164,285 to 204,078, confirming that the former number was sufficient.
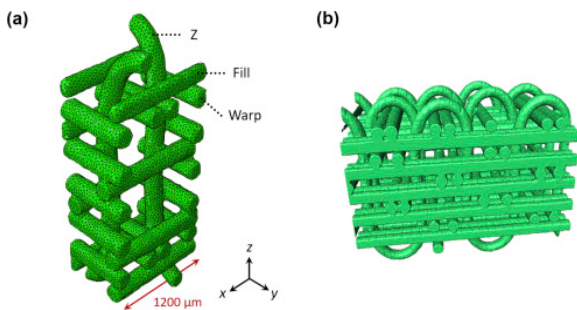

Fig. 2. (a) 3D mesh structure of the representative volume element (RVE) for a woven Ni-20Cr-3Ti-2Al superalloy, and (b) experimental microstructure obtained *via* X-ray micro-tomography [5]. The RVE has 164,285 tetrahedral elements. Total length of fill wire is 1200 μm.

The boundary conditions resulting from the creep test are enforced on the RVE, which is considered under uniaxial compressive stresses in the range of 5–50 MPa. The initial temperature of the woven structure is 825 °C, which is identical with the experimental value. The RVE has mirror boundary condition along *y* direction, and periodic boundary condition is enforced on the RVE along *x* and *z* directions. The mirror boundary condition can be specified by no displacement perpendicular to symmetry plane and no rotations along two axes in the symmetry plane while the periodic boundary condition allows nonzero displacement perpendicular to symmetry plane keeping surface elements coincident. The geometric non-linearity is considered to achieve better accuracy in the FE model.

To examine geometrical effects on the creep deformation behavior, we remove some of the Z wires and the bonds between the wires from the original woven structure, as seen in Fig. 3. Fig. 3a and b shows the modified structures without one and both Z wires, respectively, while Fig. 3c and d shows the modified structures without bounding between Z and warp wires and between Z and fill wires, respectively.
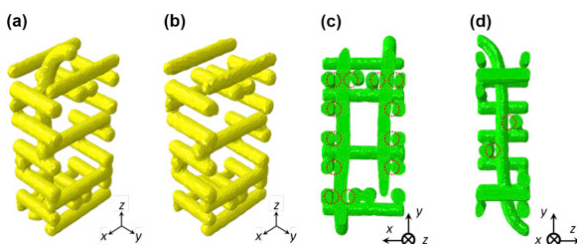
Fig. 3. Modified structures with (a) one and (b) two Z wires removed, and cross-sections showing modified structures with bonding removed (c) between Z and warp wires, and (d) between Z and fill wires. The red dotted circles indicate locations of removed bonding. (For interpretation of the references to color in this figure legend, the reader is referred to the Web version of this article.)

To simulate the creep buckling behavior, an imperfection in the form of the buckling mode (determined using a linear buckling analysis) is introduced in the initial structure, and the response of the RVE is considered under uniaxial compressive stresses in the range of 5–50 MPa at 825 °C by sequentially introducing the geometric imperfection into the FE model. We employ a method for the postbuckling analysis, as previously reported in Refs. [[29], [30], [31]], which is provided by ABAQUS/Standard software.

4. Results and discussion

4.1. Experimental results

4.1.1. Processing and microstructure

The bulk alloys and homogenized wires have average grain sizes of 220 and 80 µm, respectively. Due to the smaller grain size, a higher contribution due to diffusional creep can be expected in wire woven structures. However, given the relatively high applied stresses used during the creep tests, the dominant mechanism is expected to be dislocation creep for both grain sizes. Diffusional creep becoming dominant for the wires, due to their smaller grain size, cannot be completely excluded, however, at which point the creep rates from the bulk alloys used in the FE model are underestimated. The arc melted and aged alloys have a uniformly distributed, nearly mono-sized precipitate microstructure, as seen in Fig. 4a. The precipitates have an average size of 255 ± 60 nm and a volume fraction of 20%.
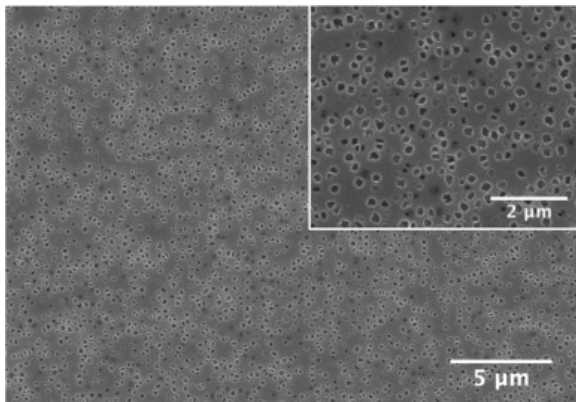

Fig. 4. SEM image showing an etched cross-section of the aged bulk Ni-based superalloy. γ' precipitates, with an average size of 255 ± 60 nm, are uniformly distributed throughout the matrix. The inset shows a micrograph with a higher magnification.

Previous research with aluminized and alumino-titanized woven structures showed minimal compositional gradient throughout the wires (in particular at bonds between wires) and no evidence of Kirkendall porosity formation [5,20]. The woven structures have a precipitate microstructure similar to the arc-melted alloys, as it is expected due to identical compositions and heat-treatment. The wires, whose diameter grew from 202 to 215 µm due to Ti and Al deposition, are bonded at the contact points due to the formation of a transient-liquid phase at 1140 °C, as previously reported in Ref. [20]. The extent of bonding is controlled by the proximity of the wires. If the wires are in close contact or if there is a minimal gap between them, then the transient liquid phase bridged this opening to form bonding. However, in the case where there is a wider gap between the

wires, then no bonding has occurred. This will have an effect on the creep behavior which is further investigated *via* FE modeling (Sec. 4.2.2).

4.1.2. Creep properties of bulk and woven Ni-based superalloys

Secondary creep strain rates of the bulk superalloy at 825 °C are shown in Fig. 1. These results are obtained from two separate samples with a 25–30 MPa offset in the applied stresses to assess repeatability of the tests and also to increase the number of data points. The γ' precipitates coarsened from 255 ± 60 to 445 ± 128 nm during the test with no evidence of rafting. These data are used in the FE model to predict the creep properties of the woven structures, which are then compared with the experimental results obtained from the woven superalloys.

Fig. 5a is an optical micrograph of the cross-section of the whole woven structure after creep deformation up to 10% total strain at 825 °C under a final applied stress of 8 MPa, showing shear deformation consistent with creep buckling from uniaxial compression along the *z*-axis (parallel to the Z wires). Partial longitudinal cross-sections of the Z-wires are visible and indicate buckling. The deformed shape, consisting of two woven layers sheared in opposite directions, induced by the creep buckling is remarkably different from the typical behavior of the woven structure under uniaxial compression, leading to relatively fast creep strain rates in the woven structure, as shown in Fig. 5b: 2×10^{-7} s^{-1} at 5 MPa, 6×10^{-7} s^{-1} at 6 MPa and 2×10^{-5} s^{-1} at 8 MPa.
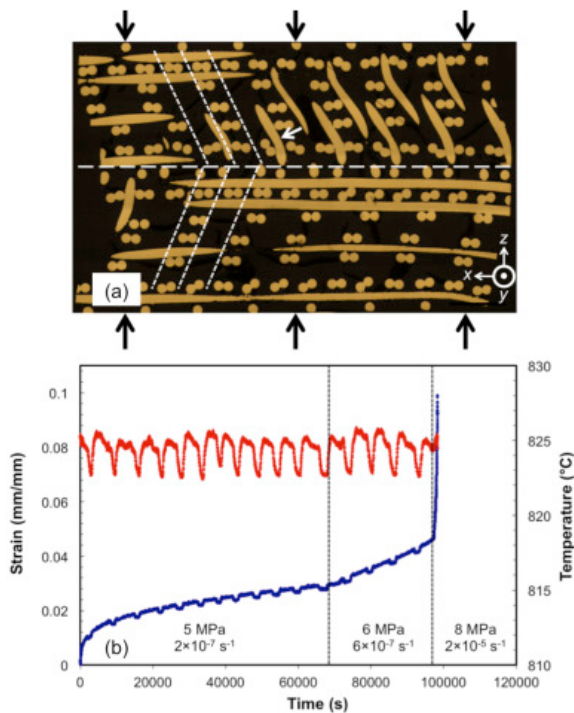

Fig. 5. (a) Optical micrograph showing the cross-section of woven Ni-20Cr-3Ti-2Al superalloy structure after creep deformation for 27 h under uniaxial compression (5–8 MPa) at 825 °C. Z wires (one of which is marked with a white arrow) have buckled with respect to the uniaxial compressive stress (vertical); the black arrows indicate the direction of uniaxial compression stress, and the dotted lines indicate the shear offset of top and bottom sections of the specimens, and (b) Measured creep strain evolution in woven Ni-20Cr-3Ti-2Al sample shown in (a), deformed under uniaxial compression (5–8 MPa) at 825 °C. Dotted lines show three different stress regions, where applied stress and resulting strain rates are indicated at the bottom of the graph. Dips are due to small (3 °C) temperature changes.

4.1.3. Static oxidation behavior of woven structures

Fig. 6 shows the square of the mass gain per unit area as a function of oxidation time for temperatures of 750, 825, and 900 °C, where the intermediate temperature is the creep test temperature used in this study. The oxidation kinetics is expected to follow a parabolic relationship [32], where the parabolic rate constant can be obtained from the slope of the linear fit for each data set. Based on this, the parabolic rate constants are 7×10^{-8}, 4×10^{-7}, and 2×10^{-6} at 750, 825, and 900 °C, respectively. Mallikarjuna et al. [32] reported that IN738LC, a polycrystalline Ni-based superalloy, has a parabolic rate constant of 2×10^{-6} at 900 °C, identical to the constant obtained for the woven structure.
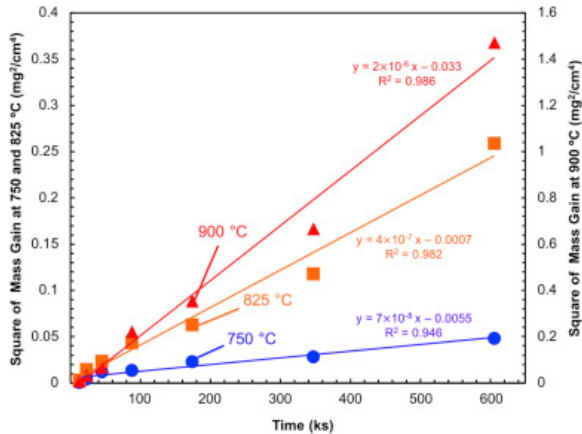
Fig. 6. Plot of square of mass gain vs time during static oxidation tests of woven structures at 750, 825, and 900 °C. The values for 900 °C are shown in the right ordinate and the other two temperatures are shown in the left ordinate. Best linear fit for each data set are shown in the graph.

The microstructures of the oxidized woven structures (after one week) are shown in Fig. 7. At 750 °C (Fig. 7a), there is a 5 μm deep oxidized layer with minimal spallation. The thickness of the oxidation layer increases to 20 μm at 825 °C (Fig. 7b) and clear evidence of intergranular oxidation is observed. There is a significant amount of spallation at the surface. The EDS maps (not shown here) suggest that chromium oxide formed at the surface and aluminum oxide at the grain boundaries. The effect of oxidation is even greater, as expected, at 900 °C (Fig. 7c). The oxide regions grow larger both at the surface and grain boundaries.
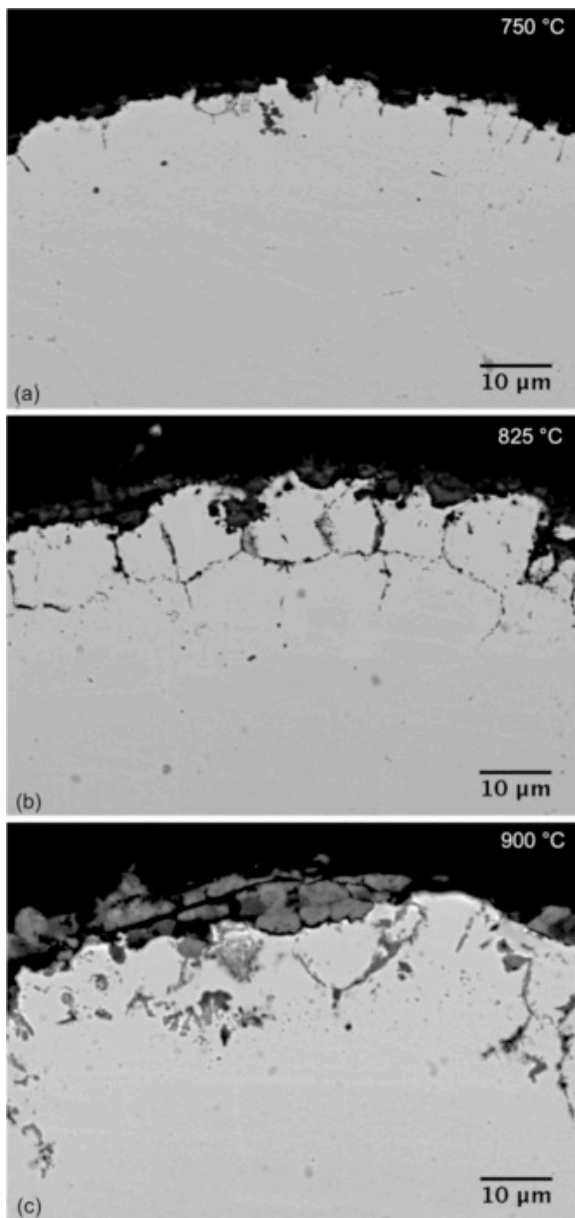
Fig. 7. SEM micrographs showing the surface of select wires in woven structures oxidized at (a) 750, (b) 825, and (c) 900 °C for 7 days.

As mentioned above, there is a 20 μm deep oxidized region in the wires at 825 °C (identical to the creep temperature) after one week (close to the average creep test duration). A 20 μm deep oxidized layer is equivalent to 35% of the cross-sectional area of each wire. Assuming that the oxidized layer has no load bearing capacity, this could mean a ~35% reduction in the load bearing capacity of the wires. This could be even more significant at the bonding regions, as these are usually smaller in size (hence relative reduction will be larger) and they transfer stress to wires perpendicular to the load. Therefore, it is critical to investigate the role of bonding regions *via* finite element analysis. Also, depositing oxidation-resistant coatings on the wires (e.g. *via* pack aluminization without final homogenization) will be beneficial for the long-term use of these woven structures at high temperatures.

4.2. Numerical results

4.2.1. Creep behavior of woven Ni-based superalloys

A typical plot of creep strain vs. time for the woven Ni-based superalloy under uniaxial compression (150 MPa along x-axis) at 825 °C is shown in Fig. 8a. The woven structures examined in this study (Fig. 8b) display a short primary-like creep region where the strain rate decreases, followed by secondary creep regime with a minimum strain rate nearly constant over an extended period of time. This primary-like creep region (despite the superalloy being considered to deform at steady state without primary creep) is a geometrical effect due to redistribution of stresses after loading and is more pronounced in the z-direction, as expected from the wire loops present at the edges of the sample which undergo bending (Fig. 8b).
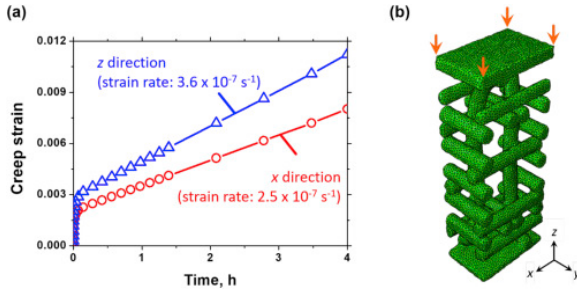

Fig. 8. (a) Computed creep strain evolution in the woven Ni-20Cr-3Ti-2Al superalloy under uniaxial compression (150 MPa) at 825 °C, and (b) 3D mesh structure of the RVE with top and bottom plates. The red and blue lines in (a) correspond to the volume average of the creep strains computed under uniaxial compression along x and z directions, respectively. The orange arrows in (b) indicate the direction of uniaxial compression stress in the z direction. (For interpretation of the references to color in this figure legend, the reader is referred to the Web version of this article.)

The power law exponent n is determined from double-logarithmic plots of secondary creep strain rate vs. stress, as shown in Fig. 9. For the woven Ni-20Cr-3Ti-2Al superalloy, n is 6.3 at 825 °C, which is identical to that for the bulk Ni-20Cr-3Ti-2Al superalloy (n = 6.3) shown in Fig. 1. It is apparent from Fig. 9 that, for a given stress, the creep strain rate for the woven Ni-based superalloy is higher by a factor of ~3.7 than that for the bulk superalloy due to the lower solid volume fraction of the woven structure, while the creep exponents are identical to both cases.
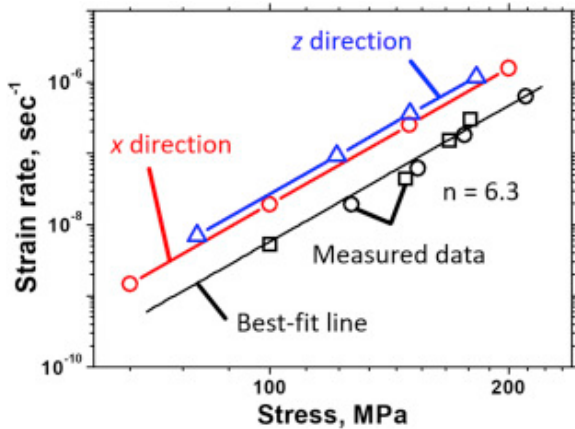

Fig. 9. Secondary creep strain rates plotted as a function of uniaxial applied stress at 825 °C for the bulk Ni-20Cr-3Ti-2Al superalloys (black data points: measured; black line: best fit). The red and blue lines correspond to the secondary creep strain rates computed for the woven structure under uniaxial compression along x and z directions, respectively. (For interpretation of the references to color in this figure legend, the reader is referred to the Web version of this article.)

To explore the effect of the applied stress direction, we compute the creep deformation under uniaxial compression along the *z*-axis, as shown in Figs. 8a and 9. In case of uniaxial compression along the *z*-axis, two flat plates are added to the RVE, as shown in Fig. 8b, since there is no flat surface along the *z*-axis due to the wire loops. The two flat plates and the wires are physically bonded. The creep strain rate in the *z* direction is higher than that computed under the *x* direction, due to the bending of the wire loops and also to the different solid fraction aligned in the load direction (as designed [9]), while the creep exponent in the both cases is nearly the same.

Stress accumulation in the woven superalloys can also be predicted from the computed results. Fig. 10 shows the von Mises stress distributions, under uniaxial compression (150 MPa) along the *x* and *z* directions, after creep at 825 °C for 4 h. As expected, the wires aligned with the load carry the majority of the stress. However, it is apparent that some load is transferred to the perpendicular wires *via* the bonds between the wires, with the bonds exhibiting strong stress concentration; this load transfer will lead to higher strength of the woven Ni-based superalloy and prevent buckling of the highly stressed wires aligned with the load. In Fig. 10, the von Mises distributions show that this load transfer from parallel to transverse wires is more pronounced for the case where the load is aligned along the *x* as compared to the *z* direction, consistent with the higher creep resistance in the former case (Fig. 9).
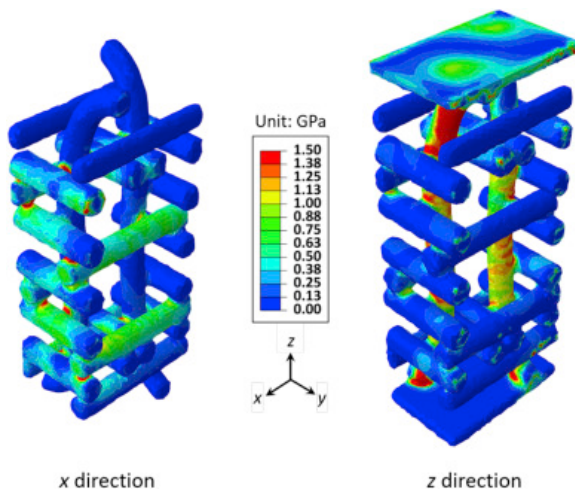

Fig. 10. The von Mises stress distributions of the woven Ni-20Cr-3Ti-2Al superalloy under uniaxial compression (150 MPa) along *x* and *z* directions at 825 °C after 4 h. The color contours correspond to surfaces of equivalent stress. (For interpretation of the references to color in this figure legend, the reader is referred to the Web version of this article.)

4.2.2. Effects of Z wires and bonds between the wires on the creep resistance

Fig. 11 shows the computed secondary creep strain rate plotted as a function of applied stress along the *x*-axis for the three cases with different number of Z wires, as illustrated in Fig. 3a and b. The computed secondary creep strain rate in the original woven structure, with all Z wires in place, is lower by a factor of ∼2.7, than those in the modified woven structure with fewer Z wires; this indicates that the Z wires, despite being perpendicular to the applied stress, are also load-bearing and thus important to the creep resistance, which is mostly controlled by the fill wires parallel to the load, that are bearing most of the load. Thus, removing both Z wires, while it decreases the relative density (to 25.5%) of the woven structure, raises the secondary creep strain rate under uniaxial compression, but does not affect creep exponent.
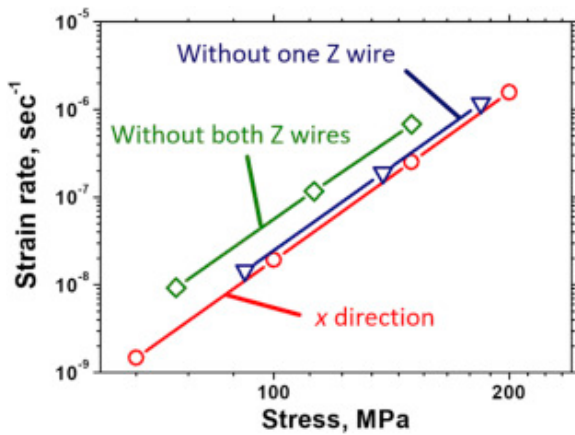
Fig. 11. Computed secondary creep strain rates plotted as a function of applied stress along *x*-axis at 825 °C for original woven structure (red). The blue and green lines correspond to the secondary creep strain rates computed in woven structures without one and both Z wires removed, respectively. (For interpretation of the references to color in this figure legend, the reader is referred to the Web version of this article.)

To further explore the geometrical effect on the creep deformation behavior of the woven structure, we artificially removed the bonding between wires from the original woven structure, as shown in Fig. 3c and d. Two cases are considered: (i) no bonding between Z and warp wires; (ii) no bonding between Z and fill wires. Fig. 12 shows the computed secondary creep strain rate plotted as a function of applied stress along *x*-axis for the two cases described above and the original woven structure. As seen in Fig. 12, the computed secondary creep strain rate in the original woven structure is lower by a factor of ~7.4 than the two modified cases. The lower creep resistance in the modified cases is due to a considerable decrease in load transfer between wires, and the corresponding increase in stress born by the wires parallel to the load, as shown in Fig. 13; nevertheless, the creep exponent in the three cases is nearly the same. The von Mises stress distributions of cross-sections for the modified structures (with bonding removed between Z and warp wires, and between Z and fill wires) indicate that there is no load transfer between wires, as seen in the black dotted circles of Fig. 13, thereby causing significant stress concentration in the fill wires that are bearing most of the load. Comparing the two debonded cases, losing bonding between Z and warp wires is less deleterious than loosing bonding between Z and fill wires. This indicates that removal of bonding between wires perpendicular to compression direction, which is equivalent to the case without bonding between Z and fill wires, results in a lower creep resistance.
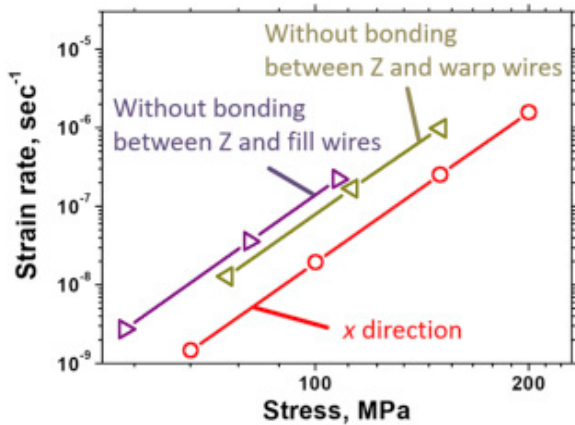

Fig. 12. Computed secondary creep strain rates plotted as a function of applied stress along *x*-axis at 825 °C for original structure (red). The ocre and purple lines correspond to the secondary creep strain rates computed for woven structures without bonding between Z and warp wires and without bonding between Z and fill wires,

respectively. (For interpretation of the references to color in this figure legend, the reader is referred to the Web version of this article.)
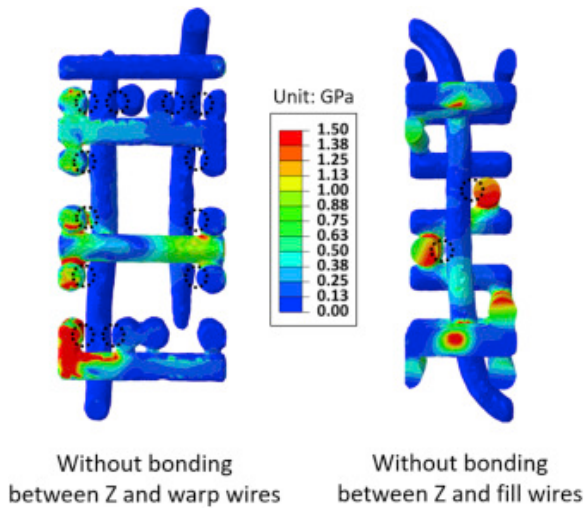

Fig. 13. The von Mises stress distributions of cross-sections showing modified structures with bonding removed between Z and warp wires (left), and between Z and fill wires (right) under uniaxial compression (150 MPa) along x direction at 825 °C after 4 h. The color contours correspond to surfaces of equivalent stress. The black dotted circles indicate locations of removed bonding. (For interpretation of the references to color in this figure legend, the reader is referred to the Web version of this article.)

4.2.3. Effect of creep buckling on the creep resistance

Buckling is characterized by the rapid lateral deflection of a high-aspect ratio structural member subjective to compressive stress. To numerically explore the effect of creep buckling on the creep deformation behavior of the woven structure, we determine one of buckling modes (determined from an eigenvalue buckling problem and closely similar to the measured deformed shape, as seen in Fig. 5a) in the woven structure using a linear buckling analysis, as seen in Fig. 14a; the geometric imperfection is imposed in the RVE by perturbations in the geometry, followed by uniaxial compression along z-axis at 825 °C. Fig. 14b shows the computed secondary creep strain rate, in the direction of the applied compressive stresses (ranging from 5 to 20 MPa at 825 °C), plotted as a function of the imperfection intensity (defined as the magnitude of the scaling factor of the buckling mode). As seen in Fig. 14b, for the woven structure without imperfection, creep buckling does not occur, and the secondary creep strain rates are very low (1.0×10^{-11}, 8.3×10^{-10}, and 6.7×10^{-8} s^{-1}, at 5, 10 and 20 MPa, respectively). Already with the second lowest level intensity, the creep rate increases by a factor of ~1.4; the increase is over three orders of magnitude for the seventh level of intensity. For comparison, the experimental creep rates (2×10^{-7}, 6×10^{-7} and 2×10^{-5} s^{-1} at 5, 6 and 8 MPa, respectively, from Fig. 5) are shown in Fig. 14. The creep stress exponent in the four FE cases shown in Fig. 14 is nearly the same and equal to the bulk value of the Ni-20Cr-3Ti-2Al superalloy (n = 6.3, Fig. 9). A stress exponent cannot be derived from the three experimental data points because, for each successive stress level, the degree of wire misalignment increases.
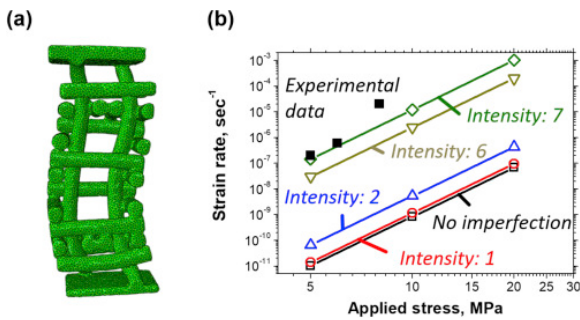
Fig. 14. (a) 3D mesh structure showing one of buckling modes determined in woven structure with stress applied along z-axis, and (b) computed secondary creep strain rate plotted as a function of intensity of imperfection under uniaxial compression in the range 5–20 MPa along z-axis at 825 °C. Experimental creep rates (from Fig. 5) are also shown.

Fig. 15 shows the computed creep strain evolutions for the woven structure without imperfection and with sixth level of intensity under uniaxial compression (20 MPa along z-axis) at 825 °C, respectively. As mentioned above, the geometrical imperfection causes the perturbations in the woven structure on the uniaxial compression, thus leading to larger amount of creep strain in the woven structure, as seen in Fig. 15. This indicates that it is important to keep the wires vertical and parallel to the uniaxial compression direction to prevent the structure from rapid failure induced by creep buckling.
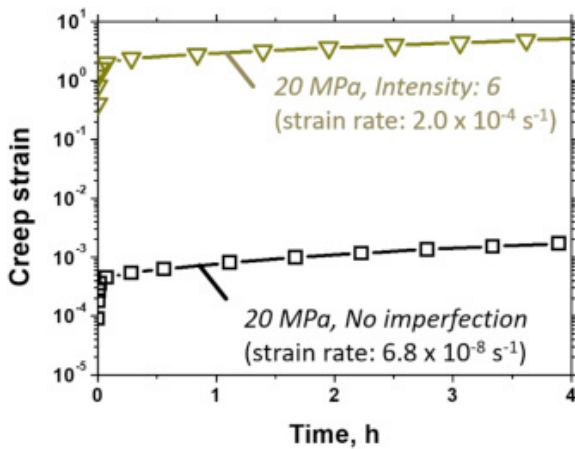

Fig. 15. Computed creep strain evolutions for the woven structure without imperfection (black line) and with sixth level of intensity (ocre line) under uniaxial compression (20 MPa) along z-axis at 825 °C.

5. Conclusions

We study experimentally the compressive creep deformation behavior of a woven structure, created from Ni-20Cr-3Ti-2Al (wt.%) superalloy wires, under uniaxial compression at elevated temperature. The woven structure exhibits a creep strain rate of 2×10^{-7} s^{-1} under an applied compressive stress of 5 MPa at 825 °C, which is much higher than expected if the wires remain parallel to the applied load. Post-creep metallography indeed shows shearing within the two woven layers, which creates strong wire misalignment with respect to the applied load. Also, the measured oxidation rates at 825 °C, while comparable to those of commercial Ni-based superalloys, are sufficient to oxidize a large fraction of the wires (35% after 168 h at 825 °C), thus reducing the creep resistance of the structures: oxidation-resistant coatings are thus particularly important for these structures with high surface to volume ratios.

We also carry out a [finite-element](#) analysis of woven structures (as previously imaged *via* micro-tomography) to predict their creep deformation behavior. We find that reducing the number of Z wires (perpendicular to the applied load) and the number of bonds between the wires (formed *via* transient [liquid phase](#) bonding) decreases creep resistance, because less load transfer is occurring from the wires parallel to the stress (and bearing most of the load) to those which are orthogonal. Additionally, creep buckling increases by orders of magnitude the creep rate of the woven structure, in qualitative agreement with the high experimental strain rate measured experimentally on the internally buckled structure with misaligned wires.

Acknowledgements

References

[1] T.A. Schaedler, A.J. Jacobsen, A. Torrents, A.E. Sorensen, J. Lian, J.R. Greer, L. Valdevit, W.B. Carter **Ultralight metallic microlattices** Science, 334 (6058) (2011), pp. 962-965

[2] M.G. Lee, J.W. Lee, S.C. Han, K. Kang **Mechanical analyses of "Shellular", an ultralow-density material** Acta Mater., 103 (2016), pp. 595-607

[3] Y. Brechet, J.D. Embury **Architectured materials: expanding materials space** Scripta Mater., 68 (1) (2013), pp. 1-3

[4] M. Ashby **Designing architectured materials** Scripta Mater., 68 (1) (2013), pp. 4-7

[5] D. Erdeniz, A.J. Levinson, K.W. Sharp, D.J. Rowenhorst, R.W. Fonda, D.C. Dunand **Pack aluminization synthesis of superalloy 3D woven and 3D braided structures** Metall. Mater. Trans. A, 46A (1) (2015), pp. 426-438

[6] M.F. Ashby **Metal Foams : a Design Guide** Butterworth-Heinemann, Boston (2000)

[7] T.J. Lu, H.A. Stone, M.F. Ashby **Heat transfer in open-cell metal foams** Acta Mater., 46 (10) (1998), pp. 3619-3635

[8] I.W. Hall, M. Guden, C.J. Yu **Crushing of aluminum closed cell foams: density and strain rate effects** Scripta Mater., 43 (6) (2000), pp. 515-521

[9]
L.Y. Zhao, S. Ha, K.W. Sharp, A.B. Geltmacher, R.W. Fonda, A.H. Kinsey, Y. Zhang, S.M. Ryan, D. Erdeniz, D.C. Dunand, K.J. Hemker, J.K. Guest, T.P. Weihs **Permeability measurements and modeling of topology-optimized metallic 3-D woven lattices** Acta Mater., 81 (2014), pp. 326-336

[10] S.H. Ha, J.K. Guest **Optimizing inclusion shapes and patterns in periodic materials using discrete object projection** Struct Multidiscip O, 50 (1) (2014), pp. 65-80

[11] K.J. Maloney, K.D. Fink, T.A. Schaedler, J.A. Kolodziejska, A.J. Jacobsen, C.S. Roper **Multifunctional heat exchangers derived from three-dimensional micro-lattice structures** Int. J. Heat Mass Tran., 55 (9–10) (2012), pp. 2486-2493

[12] D. Erdeniz, T.A. Schaedler, D.C. Dunand **Deposition-based synthesis of nickel-based superalloy microlattices** Scripta Mater., 138 (2017), pp. 28-31

[13] R.A. Wirtz, X. Jun, P. Ji-Wook, D. Ruch **Thermal/fluid characteristics of 3-D woven mesh structures as heat exchanger surfaces** IEEE Trans. Compon. Packag. Technol., 26 (1) (2003), pp. 40-47

[14] C.S. Andreasen, O. Sigmund **Saturated poroelastic actuators generated by topology optimization** Struct Multidiscip O, 43 (5) (2010), pp. 693-706

[15] V.J. Challis, A.P. Roberts, J.F. Grotowski, L.-C. Zhang, T.B. Sercombe **Prototypes for bone implant scaffolds designed via topology optimization and manufactured by solid freeform fabrication** Adv. Eng. Mater., 12 (11) (2010), pp. 1106-1110

[16] V.J. Challis, J.K. Guest, J.F. Grotowski, A.P. Roberts **Computationally generated cross-property bounds for stiffness and fluid permeability using topology optimization** Int. J. Solid Struct., 49 (23–24) (2012), pp. 3397-3408

[17] Y. Boonyongmaneerat, D.C. Dunand **Effects of strut geometry and pore fraction on creep properties of cellular materials** Acta Mater., 57 (5) (2009), pp. 1373-1384

[18] H. Choe, D.C. Dunand **Synthesis, structure, and mechanical properties of Ni–Al and Ni–Cr–Al superalloy foams** Acta Mater., 52 (5) (2004), pp. 1283-1295

[19] S.M. Oppenheimer, D.C. Dunand **Finite element modeling of creep deformation in cellular metals** Acta Mater., 55 (11) (2007), pp. 3825-3834

[20] D. Erdeniz, K.W. Sharp, D.C. Dunand **Transient liquid-phase bonded 3D woven Ni-based superalloys** Scripta Mater., 108 (2015), pp. 60-63

[21] L.J. Gibson, M.F. Ashby **Cellular Solids : Structure and Properties** (second ed.), Cambridge University Press, Cambridge ; New York (1997)

[22] R. Kossowsky **Creep behavior of Ni-Cr lamellar eutectic alloy** Metall. Trans., 1 (7) (1970), pp. 1909-1919

[23] A. Schnaas, H.J. Grabke **High-temperature corrosion and creep of Ni-Cr-Fe alloys in carburizing and oxidizing environments** Oxid. Metals, 12 (5) (1978), pp. 387-404

[24] R.W. Hayes, F. Azzarto, E.A. Klopfer, M.A. Crimp **Characterization of creep deformation of Ni-Cr solid solution alloy Nimonic 75** Mat Sci Eng a-Struct, 690 (2017), pp. 453-462

[25] Y. Ro, Y. Koizumi, H. Harada **High temperature tensile properties of a series of nickel-base superalloys on a γ/γ' tie line** Mater. Sci. Eng., A, 223 (1–2) (1997), pp. 59-63

[26] T.M. Pollock, S. Tin **Nickel-based superalloys for advanced turbine engines: chemistry, microstructure and properties** J. Propul. Power, 22 (2) (2006), pp. 361-374

[27] G.-x. Yang, Y.-f. Xu, L. Jiang, S.-h. Liang **High temperature tensile properties and fracture behavior of cast nickel-base K445 superalloy** Prog. Nat. Sci.: Mater. Int., 21 (5) (2011), pp. 418-425

[28] Z. Li, J. Xiong, Q. Xu, J. Li, B. Liu **Deformation and recrystallization of single crystal nickel-based superalloys during investment casting** J. Mater. Process. Technol., 217 (2015), pp. 1-12

[29] H.H. Cho, Y. Cho, H.N. Han **Finite element analysis for mechanical response of Ti foams with regular structure obtained by selective laser melting** Acta Mater., 97 (2015), pp. 199-206

[30] Y. Cho, T.H. Ahn, H.H. Cho, J.H. Shin, J.H. Moon, S. Yang, I.S. Choi, H.N. Han, J. Li **Study of architectural responses of 3D periodic cellular materials** Model Simul Mater Sc, 21 (6) (2013)

[31] J.T. Overvelde, S. Shan, K. Bertoldi **Compaction through buckling in 2D periodic, soft and porous structures: effect of pore shape** Adv. Mater., 24 (17) (2012), pp. 2337-2342

[32] H.T. Mallikarjuna, N.L. Richards, W.F. Caley **Isothermal oxidation comparison of three Ni-Based superalloys** J. Mater. Eng. Perform., 26 (5) (2017), pp. 2014-2023